FRONTIERS OF PHYSICS

RESEARCH ARTICLE
Volume 21 / Issue 11 / 114203 / 2026

Directionally enhanced thermoelectric effect caused by structural dislocations for in-plane heterostructures

Yuan Shang [1], Qingzhang You [2], Yuqiang Wu [1], Mengtao Sun [1,†]

1 School of Mathematics and Physics, Beijing Advanced Innovation Center for Materials Genome Engineering, University of Science and Technology Beijing, Beijing 100083, China
2 School of Science, Inner Mongolia University of Science and Technology, Baotou 014010, China
Corresponding author. E-mail: †mengtaosun@ustb.edu.cn
Received January 21, 2026; accepted March 16, 2026

ABSTRACT

Two-dimensional (2D) materials exhibit excellent thermoelectric performance attributable to their lower dimensions. Through quantum transport theoretical calculations, we find that the asymmetric Janus monolayer materials (HfSSe and ZrSSe) possess the thermoelectric advantages of two interfaces (S and Se) simultaneously at both room temperature and high temperatures. The interface effect will directionally enhance the thermoelectric figure of merit (ZT) of in-plane heterostructures along the direction perpendicular to the interface. In addition, the introduction of structural dislocations at the interface can significantly enhance the ZT value of the in-plane heterostructure in the transport along the direction parallel to the interface. At the same time, by adjusting the ratio of the two materials at the interface, the optimal ZT of the in-plane heterostructure along the transport direction parallel to the interface can be enhanced to 1.63 (3.4) at 300 K (800 K). Furthermore, we propose that employing laser ablation to fabricate vertical heterostructures into graphical superlattices can substantially decrease the lattice thermal conductivity of the structure, thereby enhancing the thermoelectric performance of the material significantly. Our study provides theoretical support for enhancing the thermoelectric performance of 2D materials.

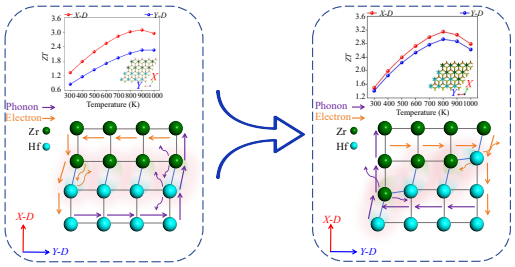

Keywords thermoelectric performance, Janus monolayer materials, interface effect, structural dislocations, graphical superlattices

1 Introduction

Thermoelectric technology provides an innovative low-carbon and renewable energy solution by converting waste heat into usable electrical power [1–4]. The core of advancing thermoelectric technology lies in enhancing the efficiency of the conversion between thermal and electrical energy. The conversion efficiency is primarily governed by the electron and phonon transport properties of the thermoelectric material, which can be quantified using the dimensionless thermoelectric figure of merit (ZT) with $ZT = S^2\sigma T/(\kappa_e + \kappa_\iota)$, where S, σ, T, κ_e and κ_ι are the Seebeck coefficient, electrical conductivity, absolute temperature in Kelvin, and electronic and lattice thermal conductivity, respectively [5, 6]. Therefore, an excellent thermoelectric material should possess both high power factor ($PF = S^2\sigma$) and low total thermal conductivity ($\kappa_{\mathrm{Tot}} = \kappa_e + \kappa_\iota$). Given the intrinsic coupling between electrical and thermal transport properties in materials, enhancing the ZT value of materials presents

https://doi.org/10.15302/frontphys.2026.114203

a significant challenge [7–10].

Identifying novel materials with higher thermoelectric performance and investigating methods to improve their ZT are two critical tasks in the field of thermoelectric research. Two-dimensional (2D) transition metal dichalcogenides (TMDs) are regarded as a promising thermoelectric material due to their excellent electronic properties and suitable thermal properties [11–13]. Whereafter, Cheng *et al.* [14] completely replaced one layer of sulfur atoms in the traditional TMDs (MX_2) with another layer of the VI element. This can significantly improve the electronic and phononic properties of the structure. They referred to this asymmetric structure as a Janus structure (MXY). In recent years, Patel et al. discovered that the Janus structure can significantly enhance the thermoelectric performance of the material [15]. They verified through theoretical calculations that the ZT value of the Janus monolayer WSTe material can reach 0.74 (2.56) at 300 (1200) K. This is mainly due to the fact that the Janus structure not only enhances its power factor but also reduces the phonon thermal conductivity. At present, researchers have discovered some two-dimensional Janus structures with relatively high thermoelectric performance, such as PdSeTe [16], InSSe [17], and WSeTe [18]. Through a series of methods, such as doping [19, 20], strain or pressure [21–24], and defect engineering [25, 26], the thermoelectric performance of 2D materials can be further enhanced. Bai *et al.* [27] have demonstrated through theoretical calculations that strain engineering can significantly enhance the thermoelectric performance of Janus materials. When strain of 4% is applied to monolayer PbSSe, the theoretical prediction of the maximum ZT is approximately 3.77 in the 900 K. At different temperatures, the improvement of the optimal ZT value by biaxial strain falls within the range of 1 to 3 times. Meanwhile, Deng *et al.* [28] demonstrated through theoretical calculations that when a 6% strain is applied to the Janus monolayer ZrSSe material, the optimal ZT value can be increased to 1.87 (3.24) at 300 (900) K, with an increase of nearly 70%. The IV group with high temperature resistance properties TMDs (HfS_2 and $HfSe_2$) exhibit superior thermoelectric performance compared to traditional VI group TMDs (MoS_2 and $MoSe_2$) [29, 30]. However, there are relatively few studies on the thermoelectric properties of such materials, and most of them enhance their ZT through strain.

Here, we designed two Janus IV group TMDs monolayer materials (HfSSe and ZrSSe). By means of first-principles calculations combined with the non-equilibrium Green's functional formalisms (NEGF-DFT), we have confirmed that both Janus monolayer materials exhibit superior thermoelectric performance, effectively integrating the thermoelectric advantages of both S and Se structured TMDs at both room and high temperatures. Meanwhile, constructing the in-plane heterostructure of the two Janus materials to enhance the ZT along the direction perpendicular to the interface of the structure through the interface effect. On the basis of this, by introducing a controlled density of structural dislocations near the interface, the ZT of the structures along the direction parallel to the interface is also significantly enhanced. Finally, for vertically stacked bilayer heterostructures, we propose a method utilizing laser ablation to construct the graphical superlattice structure, thereby enhancing their thermoelectric performance. This study provides theoretical support for enhancing the thermoelectric performance of materials through interface effects.

2 Methods

First-principles calculations. The vacuum layer larger than 15 Å was used to ensure the decoupling between the periodically repeated cells, followed by structural optimization and associated electronic state calculations performed with the Vienna Ab initio Simulation Package (VASP) software [31, 32]. First-principles calculations were performed with density-functional theory (DFT), and the Perdew–Burke–Ernzerhof (PBE) functional and generalized gradient approximation (GGA) were used [33]. The vdW interaction was considered via DFT-D3 functional [34, 35]. The spin-orbit coupling (SOC) effect is taken into account in all the primitive structures. For the unit cell (monolayer and bilayer) and supercell (heterostructure) structures, the numbers of K points are $12 \times 12 \times 1$ and $4 \times 4 \times 1$, respectively. The cutting energy is 500 eV. The forces on all atoms were less than 10^{-4} eV·Å^{-1} and the total energy converged within 10^{-6} eV.

Molecular dynamics simulation. The thermodynamic stability of the structure is simulated by ab initio molecular dynamics (AIMD) [36]. The first is to expand the protocell to a $4 \times 4 \times 1$ supercell structure. The numbers of K points are $2 \times 2 \times 1$ and the temperature range is 100 to 1000 K. The simulation time of a single step is 3 ps, and the total simulation time is 3000 ps.

Thermoelectric parameter calculation. The thermoelectric parameters of each structure were computed using the Nanodcal software. The quantum transport properties of materials were obtained through first-principles calculations in conjunction with the non-equilibrium Green's function formalism (NEGF) [37, 38]. For the calculation of static self-consistent field (SCF), the GGA-PBE96 electron exchange-correlation is used. The forces on all atoms were less than 10^{-4} eV·Å^{-1}, and the total energy converged within 10^{-6} eV. For the unit cell (monolayer and bilayer) and supercell (heterostructure) structures, the numbers of K points are $22 \times 22 \times 1$ and $8 \times 8 \times 1$, respectively. For the calculation of thermoelectric parameter properties, the numbers of K points are $25 \times 25 \times 1$. Under this criterion, for all structures, the variation

of ZT at higher K-point densities does not exceed 0.1, and the changes in other related thermoelectric parameters are less than 10^{-2}. All the data calculations were repeated multiple times, and the values did not change. In this work, we can obtain the electrical conductivity (σ), the Seebeck coefficient (S), and the electronic thermal conductivity ($\kappa_e(T)$):

$$\sigma = \frac{e^2 L_0}{l}, \tag{1}$$

$$S = -\frac{L_1}{eTL_0}, \tag{2}$$

$$\kappa_e(T) = \frac{1}{Tl}\left(L_2 - \frac{L_1^2}{L_0}\right), \tag{3}$$

where e is the elementary charge, l is the device length (the length l of each device is the optimized primitive unit cell lattice constant in the transport direction of the structure, respectively), T is the absolute temperature in kelvin, and $L_m(\mu)$ is given by

$$L_m(\mu) = \frac{2}{h}\int_{-\infty}^{\infty} \mathrm{d}\varepsilon T_\mathrm{e}(\varepsilon)(\varepsilon-\mu)^m\left(-\frac{\partial f(\varepsilon,\mu)}{\partial\varepsilon}\right), \tag{4}$$

where h is the Planck constant, μ is the chemical potential, $T_\mathrm{e}(\varepsilon)$ is the electron transmission spectrum, and $f(\varepsilon,\mu)$ is the Fermi energy distribution function. The phononic thermal conductivity can then be achieved by

$$\kappa_p(T) = \frac{\hbar^2}{2\pi k_\mathrm{B} T^2 l}\int_0^{\infty} \mathrm{d}\omega\omega^2 T_\mathrm{p}(\omega)\frac{\mathrm{e}^{\frac{\hbar\omega}{k_\mathrm{B}T}}}{\left(\mathrm{e}^{\frac{\hbar\omega}{k_\mathrm{B}T}}-1\right)^2}, \tag{5}$$

where $\hbar$ is the reduced Planck constant, k_B is the Boltzmann constant, ω is the phonon angular frequency, and $T_\mathrm{p}(\omega)$ is the phonon transmission function.

3 Results and discussion

3.1 Electronic and thermoelectric properties of Janus monolayer materials

The top (or bottom) S atoms in MS_2 (M = Hf/Zr) monolayer are replaced by Se atoms to form a Janus monolayer materials MSSe (M = Hf/Zr), it belongs to the P3m1 space group and side (top) view as shown in Fig. 1(a). Owing to the different atomic layers present above and below the material, it exhibits more intricate properties [39, 40]. The charge densities and the average electrostatic potentials along the z direction for both Janus monolayer materials HfSSe and HfS_2 ($HfSe_2$) is illustrated in Fig. 1(b). The Janus monolayer material HfSSe has an asymmetric mean electrostatic potential in the z direction because the charge densities of the S and Se atoms are not the same, and the lower potential energy near the S atom also means that the charge density here is higher. Figures 1(c, d) illustrate the projected energy band of the atomic orbitals and effective mass of Janus monolayer materials ZrSSe and HfSSe (M-ZrSSe and M-HfSSe) with the spin–orbit coupling (SOC) effect. The band structures of the two materials exhibit similarities, and both belong to indirect bandgap semiconductors with a band energy of 0.567 (M-ZrSSe) and 0.645 (M-HfSSe) eV, respectively. The high symmetric points of both materials at the valence band maximum (VBM) and conduction band minimum (CBM) are Γ and M, respectively; which are composed of the $p_x + p_y$ orbital of Se atom and the d_{z^2} orbital of Zr/Hf atom. The effective mass is a critical parameter that characterizes the transport properties of material [41]. It usually exhibits a proportional relationship with the S. The effective masses of both M-ZrSSe and M-HfSSe materials exhibit significant anisotropy at the CBM, and the electron effective masses in the M→Γ (M→K) direction are 2.167 (0.263) and 2.447 m_e (0.222 m_e), respectively. Both materials exhibit the large electron effective mass at the CBM, so they possess a high density of states (DOS) at the CBM (Fig. S1). These characteristics suggest that both materials have the potential to be the N-type thermoelectric materials with a high S.

The thermodynamic and structural stability of both M-ZrSSe and M-HfSSe materials were established through ab initio molecular dynamics (AIMD) simulations conducted at a temperature of 1000 K, as well as phonon dispersion analysis across the entire Brillouin zone [Figs. S2(a, b)]. Subsequently, we computed the change in ZT of the two materials at different temperatures with the chemical potential [Fig. S2(c)]. The function diagram of the optimal ZT with temperature were drawn, and compared these results with non-Janus materials, as illustrated in Fig. 1(e). The S-based and Se-based materials exhibit excellent thermoelectric performance at high temperatures and room temperatures (300 K), respectively. The Janus monolayer materials effectively integrate the thermoelectric advantages of two type of interfaces at both room temperature and high temperatures, thereby, it more suitable for practical applications. The optimal ZT of M-ZrSSe (M-HfSSe) is 0.88 (0.99) at room temperature and reaches the highest 2.31 (2.74) at 900 K. It is evident that the thermoelectric performance of M-HfSSe exceeds that of M-ZrSSe, which is one of the better thermoelectric materials in Janus materials (Table S1). We calculate the thermoelectric parameters associated with the optimal ZT at room temperature of the two materials (all thermoelectric parameters are taken as absolute values), and scale them to a suitable scale in the radar diagram, as shown in Fig. 1(f). The other thermoelectric parameters value of M-ZrSSe, with the exception of the S, are all higher to

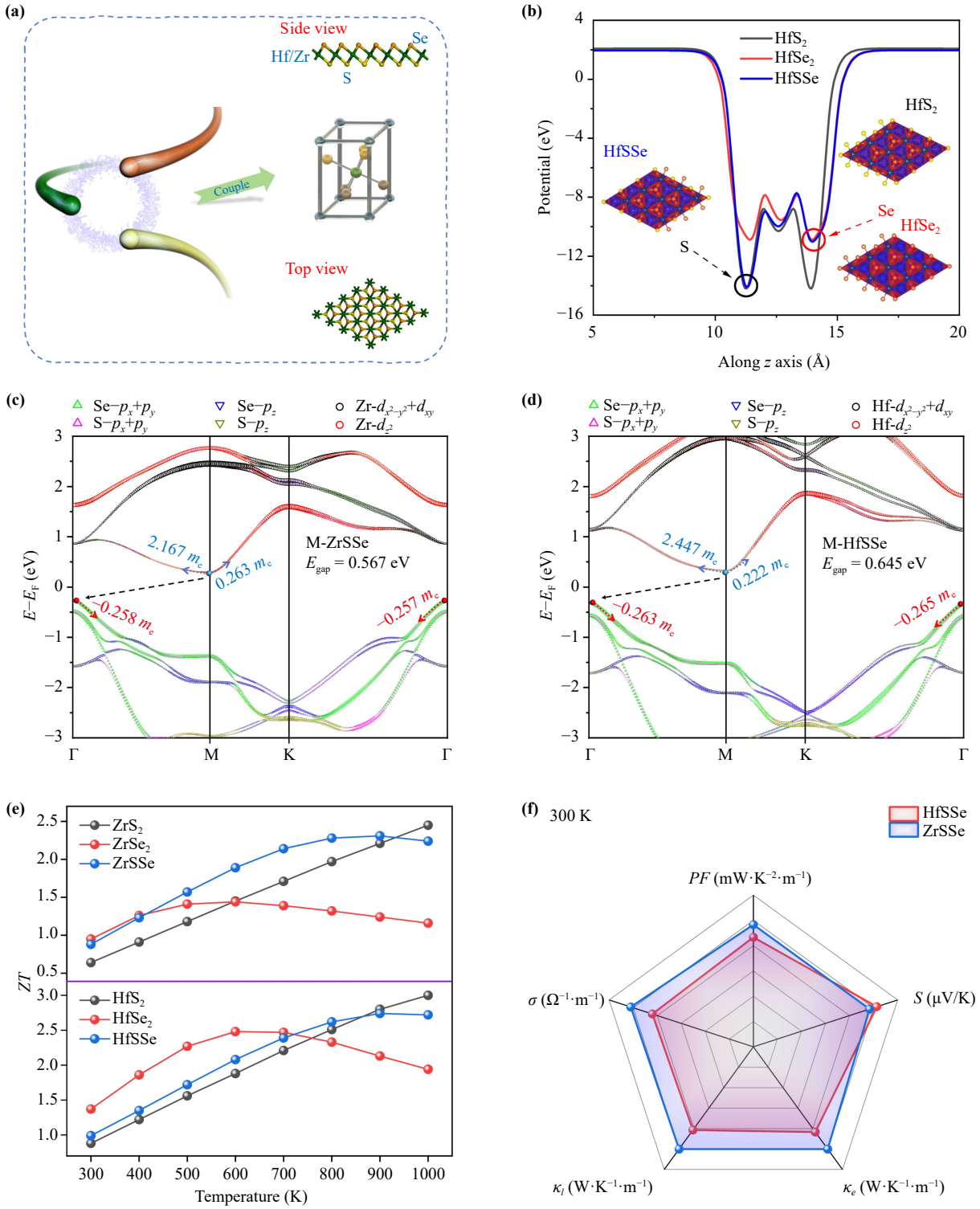

Fig. 1 Crystal structure, electronic band characteristics, and thermoelectric properties of Janus monolayer materials. **(a)** Schematic diagram of the atomic composition structure of the Janus monolayer materials and the top and side view of crystal structure. **(b)** The average electrostatic potential energy along the z axis of monolayer materials HfSSe, HfS_2 and $HfSe_2$, and the illustration for charge densities [the blue (red) color represents the charge density of the electron (hole)]. **(c)** M-ZrSSe; **(d)** M-HfSSe are projected energy band of the atomic orbitals of the materials, and the blue and red spheres represent electron and hole, respectively. **(e)** The optimal ZT of Janus monolayer materials (M-ZrSSe and M-HfSSe) and their corresponding non-Janus (M-ZrS_2/$ZrSe_2$ and M-HfS_2/$HfSe_2$) counterparts as a function of temperature. **(f)** The radar comparison of thermoelectric parameters associated with optimal ZT at room temperature (300 K) for M-ZrSSe and M-HfSSe (scaled by an appropriate ratio, and all physical parameters are taken as absolute values).

than those of M-HfSSe. At 300 K, the S and κ_ι of M-ZrSSe are –223 μV/K and 0.23 $W{\cdot}K^{-1}{\cdot}m^{-1}$, and those of M-HfSSe are –237 μV/K and 0.19 $W{\cdot}K^{-1}{\cdot}m^{-1}$. This is mainly due to the fact that Hf atoms have a large effective mass and a low phonon group velocity, resulting in a higher S and a lower κ_ι [42].

3.2 Impact of interface effects on thermoelectric properties of in-plane heterostructures

Combining two monolayer materials to form an in-plane heterostructure can effectively enhance the thermoelectric performance of the two materials [43, 44]. The 4×4 supercell in-plane heterostructure (M-HfSSe@ZrSSe) synthesized by two Janus monolayer materials was constructed [Fig. S3(a)], and the projected energy band of the atomic is illustrated in Fig. 2(a). The two materials will undergo charge transfer at the contact interface [Fig. S3(b)], and the in-plane heterostructure will also become a direct bandgap semiconductor with a band energy of 0.704 eV. The VBM and CBM of the structure are at the high symmetric point Γ, which is mainly composed of the Se atom and the Zr atom. It also has a high asymmetric electron effective mass at the CBM. The symmetry of the in-plane heterostructure formed by two Janus monolayer materials will be altered in comparison to that of monolayer materials, resulting in the formation of two distinct thermoelectric transport channels: one perpendicular direction (X-D) and one parallel direction (Y-D) to the contact interface between the two materials. The change in ZT of these two transport directions of the in-plane heterostructure at different temperatures with the chemical potential was calculated [Fig. S3(c)], respectively, and the function diagram of the optimal ZT with temperature were drawn, as shown in Fig. 2(b). The in-plane heterostructure is an anisotropic N-type thermoelectric material. The thermoelectric performance of the in-plane heterostructure exhibits significantly higher ZT along the X-D compared to the Y-D, and the optimal ZT of the material along the X-D (Y-D) reaches 1.33 (0.85) at room temperature and peaks at 3.09 (2.66) at 900 K. The underlying physical mechanism can be elucidated by comparing the thermoelectric parameters associated with the optimal ZT at room temperature in both directions, as illustrated in Fig. 2(c). Except for the S, the other thermoelectric parameters along the X-D are smaller than in the Y-D. At 300 K, the S and κ_ι of the X-D are –254 μV/K and 0.11 $W{\cdot}K^{-1}{\cdot}m^{-1}$, and those of the Y-D are –227 μV/K and 0.25 $W{\cdot}K^{-1}{\cdot}m^{-1}$. Compared to classical thermodynamic theory, which emphasizes that the transport properties of materials are determined by their intrinsic properties (Supplementary Text: Section S1. The classic equations), quantum transport theory underscores the significance of the transmission coefficient ($T_e(E)$), which is also the important factor affecting the current and phonon heat flow (Supplementary Text: Section S2. Quantum transport properties). For in-plane heterostructures, except for their own band structure, the main reason affecting their transmission spectra is the interface effect caused by lattice mismatch along the transport direction. It is reflected in the self-energy term of the Green's function and affects the transmission coefficients of electrons and phonons ($T_{e/p}(E)$). The motion of current and phonon heat flow along the two directions within the in-plane heterostructure is illustrated in Fig. 2(d). The movement of electrons and phonons along the Y-D direction is all within the same material, and there is no such interface effect. However, their movement along the X-D direction will pass through one material to another, which will introduce an interface effect. The reflection caused by interface effects will reduce the transmission coefficients of electrons and phonons $T_{e/p}(E)$, this results in a decrease in the σ and κ_ι, and increase in the S of the in-plane heterostructure along the X-D. Therefore, for the in-plane heterostructure, the ZT along the X-D is much higher than that along the Y-D and the thermoelectric performance of the material will show anisotropy.

Owing to the lattice mismatch, a large number of structural dislocations are generated at the interface, which will also significantly affect the thermoelectric properties of the material [45, 46]. In actual experiments, it is very difficult to study the influence of this type of structural dislocation on the thermoelectric properties of materials in isolation. Therefore, based on different structural dislocations density (α), the 4×4 in-plane heterostructures composed of M-ZrSSe and M-HfSSe were designed, as illustrated in Fig. 2(e). Each structure ensures that the number of atoms of the two materials is the same and the structural dislocations density is defined as $\alpha = n/4$. The n represents the number of structural dislocations of X (X = Hf/Zr) atoms at the interface. When the α =50%, two distinct arrangements of crystal structures may be constructed. As the α increases, the total free energy of the optimized structure also rises. All band structures with structural dislocations exhibit characteristics similar to structure without structural dislocations (α =0%), they are all direct bandgap semiconductors and the band energy decreases as the a increases (Fig. S4).

The function diagram of the optimal ZT of these two transport directions of each structure with temperature were drawn, as shown in Fig. 2(f). The impact of structural dislocations on the ZT of the in-plane heterostructures varies significantly between the two directions. For along the X-D, structural dislocations of influence on the ZT of the in-plane heterostructures are very limited. However, for along the Y-D, structural dislocations notably enhance the ZT of the in-plane heterostructures. The optimal ZT of the $\alpha = A$–50% structure is as high as 1.5 at room temperature and the optimal ZT exceeds

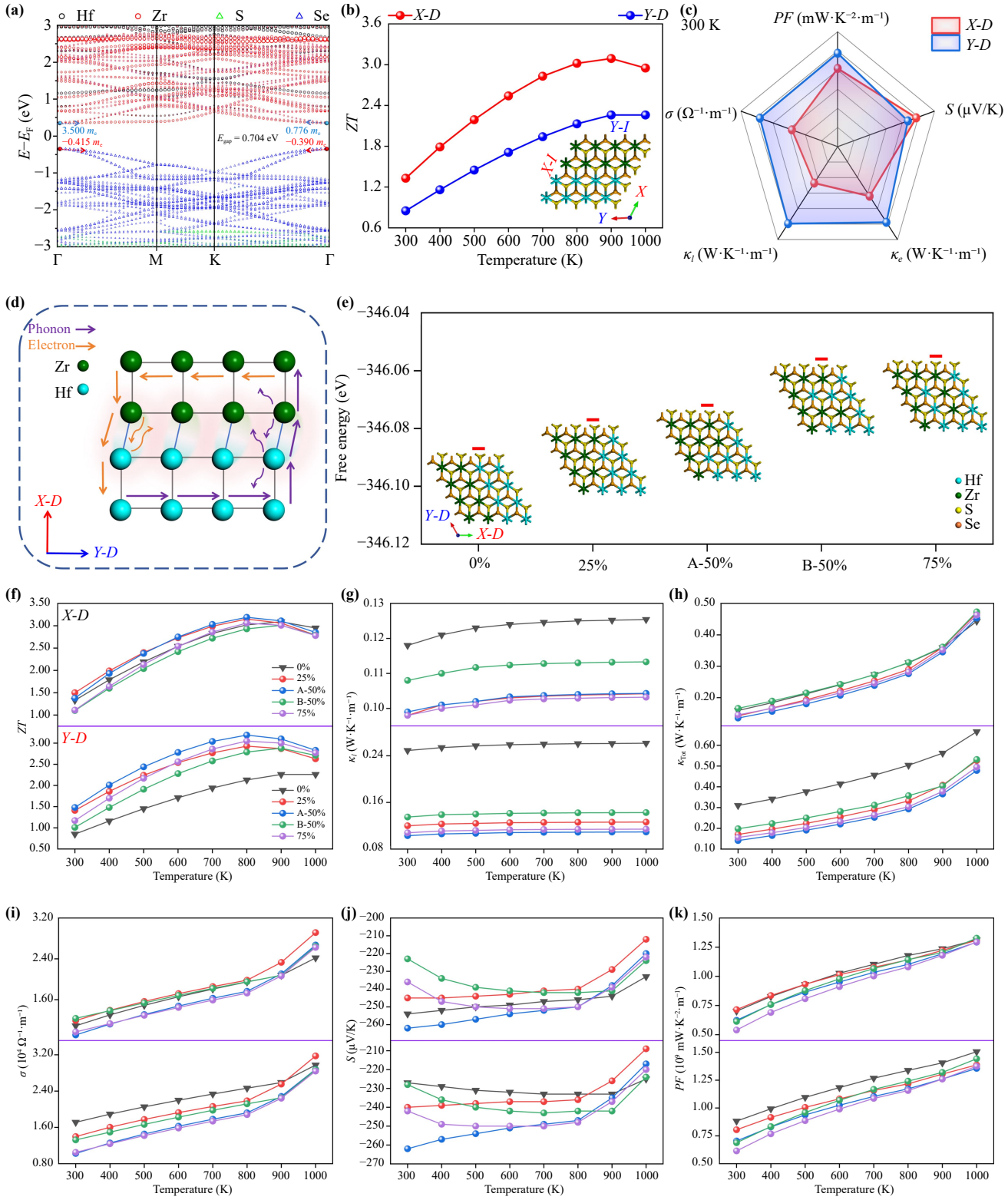

Fig. 2 Crystal structure, electronic band characteristics, and thermoelectric properties of the in-plane heterostructure composed by two Janus monolayer materials with and without structural dislocations. The in-plane heterostructure; **(a)** projected energy band of the atomic; **(b)** function diagram of optimal ZT with temperature in two transport directions (X-l and Y-l are respectively the lengths l of the structure in each transport direction); **(c)** thermoelectric parameters related to optimal ZT at room temperature; **(d)** motion situation of electron and phonon in two transport directions. The in-plane heterostructure with and without structural dislocations; **(e)** crystal structure; function diagram of **(f)** optimal ZT; **(g)** κ_l; **(h)** κ_{Tot}; **(i)** σ; **(j)** S and **(k)** PF with temperature in two transport directions.

3 at 800 K, and the temperature condition of peak ZT is also reduced. Therefore, we focus on the physical mechanism by which structural dislocations significantly enhance ZT along the *Y-D*. The κ_ι and κ_{Tot} of these two transport directions of each structure as a function of temperature are illustrated in Figs. 2(g, h) respectively. The presence of structural dislocations can significantly diminish the κ_ι of the in-plane heterostructure, with the most pronounced effect observed along the *Y-D* direction, where the reduction can exceed 50%. When structural dislocations occur, the current and phonon heat flow along the *Y-D* direction traverses two materials, and it is influenced by interface effects on both sides of the interface (Fig. S5). The acoustic branch modes in phonon vibration modes in the same material exhibit a higher group velocity compared to the optical branch modes, which is the crucial factor to determine the thermal conductivity of the lattice [47, 48]. The structures with structural dislocations exhibit a lower phonon group velocity in the acoustic branch (Fig. S6), which reduces the κ_ι. The σ and S of these two transport directions of each structure as a function of temperature are illustrated in Figs. 2(i, j), respectively. Similarly, the structural dislocations substantially reduce the σ while enhancing the S along the *Y-D*, but it exerts little influence on these two thermoelectric parameters along the *X-D*. The DOS of the band structure of each structure at the CBM also affects these two thermoelectric parameters (Fig. S4). The PF of these two transport directions of each structure as a function of temperature are illustrated in Fig. 2(k). For along the *Y-D*, the σ caused by structural dislocations makes the PF much lower than that of structure without dislocations. In summary, structural dislocation significantly enhances the ZT value of the in-plane heterostructure along the *Y-D*. This enhancement is primarily attributed to the increase in the reflectivity of phonons and electrons caused by interface effects, which reduces the κ_{Tot}. But for along the *X-D* direction, the change of ZT is mainly influenced by changes in the band and phonon structure.

The different atomic proportions of structural dislocations near the interface can affect the thermoelectric properties of the material by influencing the electronic and phononic properties [49, 50]. Therefore, based on different Zr atom ratio (β), it is defined as $\beta = n/16$, n represents the total number of Zr atoms, the 4×4 superlattice in-plane heterostructure composed of M-ZrSSe and M-HfSSe was designed, as illustrated in Fig. 3(a). These four structures can be categorized into two groups: rich Hf atoms (β =25% and β =37.5%) and rich Zr atoms (β =75% and β =62.5%). The corresponding band structure and DOS are calculated (Fig. S7), and the total free energy and band energy of the structure gradually increases and decrease with the increase of β. The interface of β =25% and β =75% structures are consistent with that of α =0% structure, there are no structural dislocations at the interface. The phonon and electron do not have interface scattering along the *Y-D* (Fig. S8). The β =37.5% and β =62.5% structures have structural dislocations that allow phonons and electrons to reflect easily along the *Y-D* in one side interface, as shown in Fig. 3(b). The structural dislocation at the interface should enhances the ZT along the *Y-D* for both structures. The function diagram of the optimal ZT along the *Y-D* of each structure with temperature was drawn, as shown in Fig. 3(c). At room temperature, the ZT of structures without structural dislocations are found to be lower compared to structures with structural dislocations, and the structures with rich Hf atoms have higher ZT than those with rich Zr atoms. The β =37.5% structure is exhibiting the highest ZT, it is 1.63 at room temperature and which increases to a maximum of 3.4 at 800 K, whereas the β =75% structure demonstrates the lowest ZT. The κ_ι and κ_{Tot} of each structure as a function of temperature are illustrated in Figs. 3(d, e), respectively. The β =75% and β =37.5% structures exhibit the highest and lowest κ_ι, respectively. Moreover, despite the presence of structural dislocations, the κ_ι of the β =62.5% structure remains higher than that of the β =25% structure, which without structural dislocations. This may be although rich Zr structures with structural dislocations have interface effects, the overall group velocity of the rich Zr structure is higher than that of the rich Hf structure due to the higher group velocity of Zr atoms compared to Hf atoms (Fig. S9). This ultimately leads to a higher κ_ι in the rich Zr structure. The κ_{Tot} is also predominantly governed by the κ_ι. The σ and S of each structure as a function of temperature are illustrated in Figs. 3(f, g), respectively. At room temperature, the structures with rich Hf atoms exhibit higher S and lower σ, and structural dislocations significantly enhance the S while reducing the σ. This is consistent with the results obtained above. Meanwhile, the absolute value of S of the structures without structural dislocations initially increases and subsequently decreases with rising temperature, whereas the absolute value of S of the structure with structural dislocations exhibits a continuous decrease with rising temperature. The higher σ of the structures with rich Zr atoms also makes them have a higher PF, as shown in Fig. 3(h). Therefore, when the two materials form the in-plane heterostructure, an increased concentration of Hf atoms at the interface and constructed structural dislocations will both significantly enhance the ZT of the heterostructure along the *Y-D*.

3.3 Electronic and thermoelectric properties of vertical heterostructures

When two Janus monolayer materials are stacked vertically, either separately or against each other, a vertical bilayer homostructure (B-HfSSe and B-ZrSSe) or

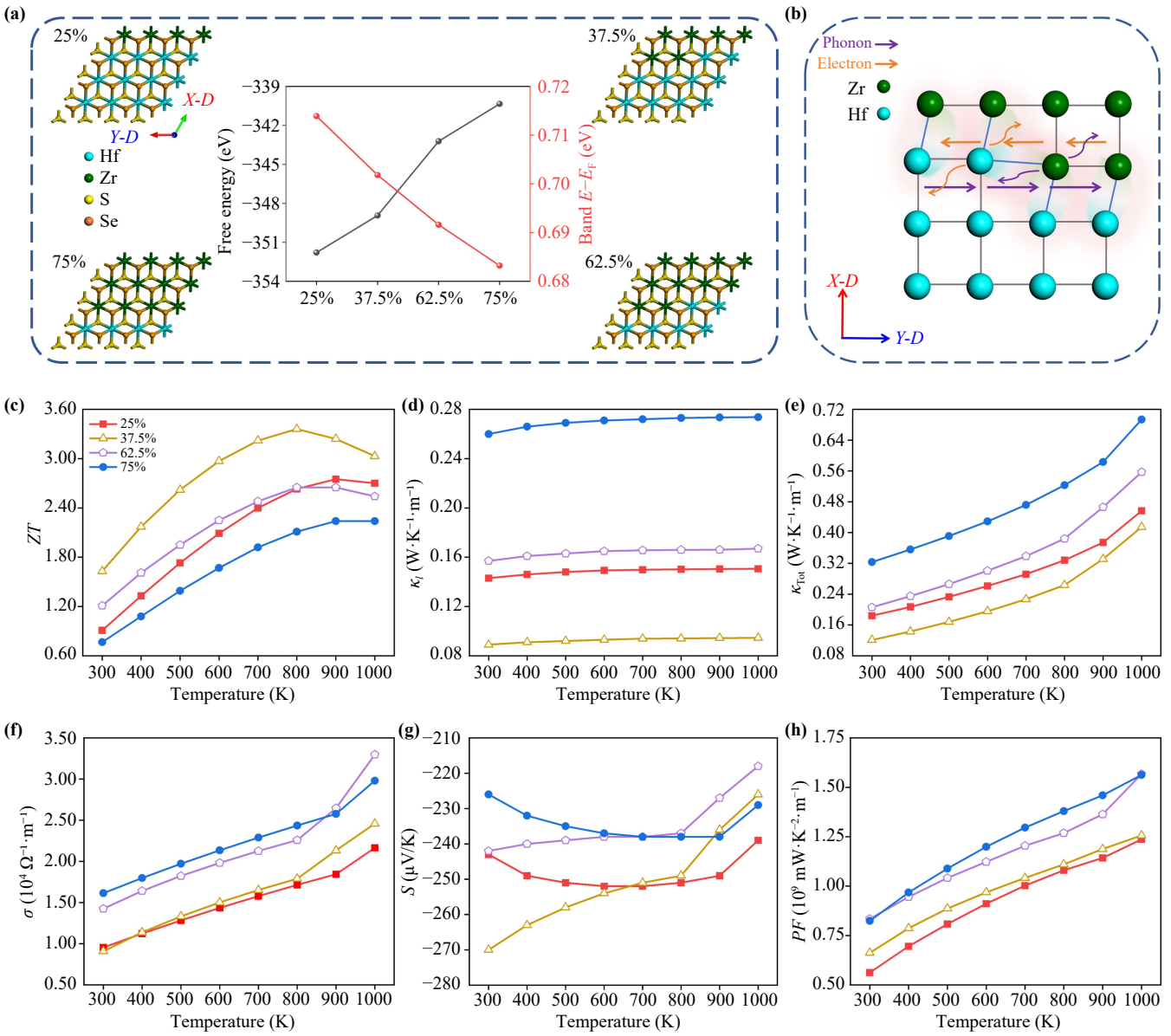

Fig. 3 Crystal structure and thermoelectric properties of the in-plane heterostructure composed by two Janus monolayer materials with rich Hf and Zr atoms. **(a)** Crystal structure of in-plane heterostructure composed by two Janus materials with rich Hf and Zr atoms, and the central diagram illustrates the band energy and total free energy of each optimized structure. **(b)** Motion situation of electron and phonon along the *Y-D* of in-plane heterostructure with rich Hf atoms. Function diagram of **(c)** optimal *ZT*; **(d)** κ_ι; **(e)** κ_{Tot}; **(f)** σ; **(g)** *S* and **(h)** *PF* with temperature along the *Y-D*.

heterostructure (B-HfSSe@ZrSSe) can be formed [51, 52]. According to previous reports, the stacking method depicted in Fig. 4(a) exhibits the lowest total free energy and possesses the most stable structure [53]. Simultaneously, based on the distinct types of atoms at the interface where the two Janus monolayer materials come into contact, these can be categorized into three modes (S-S, S-Se and Se-Se). Among them, Se-Se and S-S modes have the lowest and highest total free energy after structural optimization, respectively. The lattice constant of the vertical heterostructure following structural optimization is illustrated in Fig. 4(b). With the exception of interlayer distance (*D*), the lattice constant for S-S modes and Se-Se are essentially identical. Consequently, interlayer distance emerges as the predominant parameter influencing structural total free energy. The S-Se mode exhibits the smallest lattice constants (a, b), moderate interlayer distance, and the largest internal angles of bond (Hf_θ: S-Hf-Se, Zr_θ: S-Zr-Se), so we will focus on this contact mode. The band structure of the vertical heterostructure of S-Se mode is illustrated in Fig. 4(c). The VBM and CBM are both contributed by M-ZrSSe, thus forming a Type I heterostructure [Fig. S10(b)]. It is an indirect bandgap semiconductor with a band energy

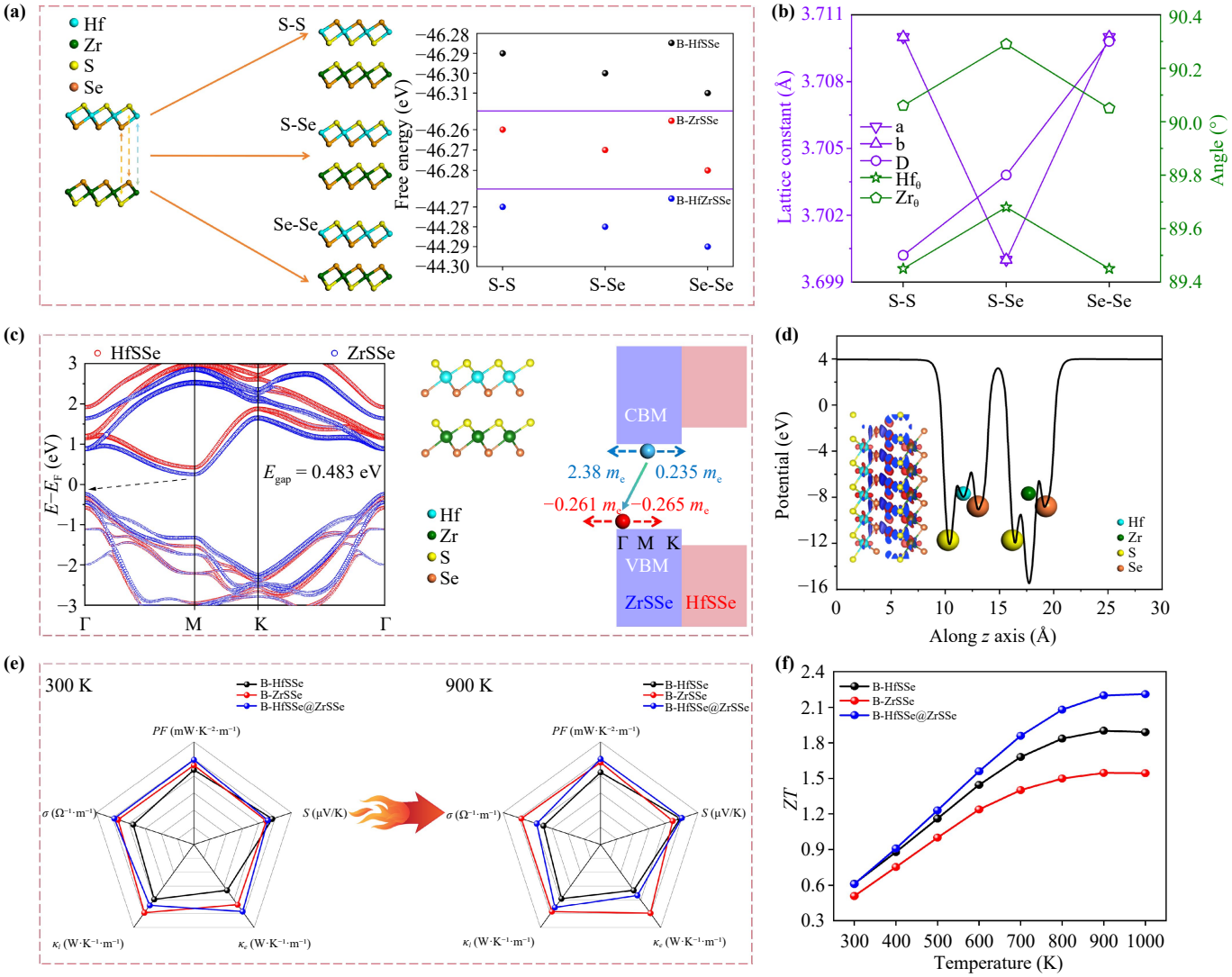

Fig. 4 Crystal structure, electronic band characteristics, and thermoelectric properties of the vertical heterostructure and homostructure. **(a)** Crystal structure of three interface modes of vertical heterostructures, and the picture on the right shows the total free energy of the heterostructure and homostructure after optimization for the three interface modes. **(b)** Lattice constants of heterostructure after optimization for the three interface modes. The heterostructure for S-Se interface modes; **(c)** band structure; **(d)** the average electrostatic potential energy along the z axis, and the illustration on the left shows charge densities. The heterostructure and homostructure for S-Se interface modes; **(e)** thermoelectric parameters related to optimal ZT at room temperature and 900 K; **(f)** function diagram of optimal ZT with temperature.

of 0.483 eV and the high electron effective masses of materials in the M→Γ (M→K) direction are 2.38 (0.235) m_e, these parameters are similar to those of M-ZrSSe material. The charge densities and the average electrostatic potentials along the z direction for the vertical heterostructure is illustrated in Fig. 4(d). The charge transfer occurs from the Se atom, which possesses a higher electrostatic potential in M-HfSSe, to the S atom with a lower electrostatic potential in M-ZrSSe. The special asymmetric electrostatic potential phenomenon of the Janus materials can be seen in the z direction. The phonon dispersion spectra and AIMD simulations indicate that the vertical heterostructure exhibits both structural and thermodynamic stability [Fig. S10(a)]. We computed the change in ZT of the vertical homostructure and heterostructure at different temperatures with the chemical potential [Fig. S10(c)]. The function diagram of the optimal ZT of each structure with temperature was drawn, as illustrated in Fig. 4(f). The vertical heterostructure is an N-type thermoelectric material that exhibits an optimal ZT of 0.611 at room temperature and an optimal ZT of 2.2 at 900 K. In comparison to the vertical homostructures, the vertical heterostructure demonstrates superior overall thermoelectric performance. Figure 4(e) illustrates the thermoelectric parameters associated with optimal ZT at room

temperature and 900 K. In comparison to the vertical homostructures, the S of the vertical heterostructure is significantly enhanced during the heating process, whereas σ is diminished. Despite this reduction in the σ, the PF of the vertical heterostructure remains superior to that of the other two vertical homostructures, and the κ_e is substantially reduced. Consequently, the thermoelectric performance of the vertical heterostructure markedly surpasses that of the vertical homostructures at high temperatures.

3.4 Impact of graphical superlattice on thermoelectric properties of vertical heterostructures

The interface of the vertical heterostructure is located in the out-of-plane direction (z); therefore, the influence of the interface scattering on the thermoelectric performance of the in-of-plane direction (x and y) of the material is relatively limited [54]. We propose a method for constructing the graphical superlattice through laser ablation of the upper material, thereby enhancing the thermoelectric performance of the vertical heterostructure at room temperature. By controlling the laser power and exposure duration, it is possible to ablate only the top layer material without impacting the bottom layer material [55, 56]. Through precise adjustment of the laser spot position, the specialized graphical superlattice structure can be fabricated, as illustrated in Fig. 5(a). The top material (M-ZrSSe) consists of a single primitive cell, while the bottom material (M-HfSSe) comprises four distinct primitive cell structures (1×1, 2×2, 3×3 and 4×4) to simulate the lattice structure following laser ablation. The corresponding band structure and DOS are calculated (Fig. S11), and defect levels can be observed in the energy bands of the latter three structures. Because of the symmetry of the structure in plane, these structures are all isotropy thermoelectric materials. The function diagram of the optimal ZT of each structure with temperature was drawn, as shown in Fig. 5(b). The graphical superlattice structure can substantially enhance the ZT at room temperature; specifically, when the 13 structure is implemented, the ZT increases from an original 0.61 to 0.85. The κ_ι and κ_{Tot} of each structure as a function with temperature are illustrated in Figs. 5(c, d), respectively. According to quantum transport theory, the κ_ι depends not only on the group velocity and transmittance coefficient of phonon vibrations but also exhibits an inverse relationship with the lattice size ($\kappa_p \propto 1/l$). Therefore, the graphical superlattice structure can reduce the κ_ι by increasing the overall size of the structure. The κ_{Tot} of each structure at room temperature is predominantly influenced by the κ_ι. The σ and S of each structure as a function with temperature are illustrated in Figs. 5(e, f), respectively. The graphical superlattice structure can decrease the σ of the structures while exerting a relatively minor influence on the S. This is because in quantum transport theory, the lattice size is also inversely proportional to the σ ($\sigma \propto 1/l$), but it does not directly affect the S. The lower σ of the graphical superlattice structure also results in a lower PF, as shown in Fig. 5(g). Therefore, the thermoelectric performance of the vertical heterostructure at room temperature can be enhanced by constructing a graphical superlattice structure (the thermoelectric performance of the graphical superlattice structure of top material (M-HfSSe) and bottom material (M-ZrSSe) can be seen in Fig. S12). This is attributed to the significantly reduced κ_{Tot} resulting from the larger lattice size, which operates under the similar physical principle as interface engineering in improving thermoelectric performance.

4 Conclusions

We prove that the interface effect can directionally enhance the thermoelectric ZT of heterostructures. By means of first-principles calculations combined with the non-equilibrium Green's functional formalisms (NEGF-DFT), we have demonstrated that Janus IV group TMDs materials (M-HfSSe and M-ZrSSe) integrate the thermoelectric advantages of two different interface elements (S and Se). This characteristic renders Janus monolayer materials excellent thermoelectric materials at both room temperature and higher temperatures. Subsequently, construction of the in-plane heterostructure composed of two Janus monolayer materials to enhance the thermoelectric ZT of the material through the interface effect. The optimal ZT of the in-plane heterostructure is enhanced to 1.33 at room temperature along the direction perpendicular to the interface. This is mainly because the interface effect enhances the reflectivity of phonons in their direction of motion, which greatly reduces the κ_l. Based on these, we designed the structural dislocations of specific density at the interface. This increases the ZT of the heterostructures at room temperature along the direction parallel to the interface to 1.5. Simultaneously, by modulating the proportion of Hf atoms at the interface, the ZT value can be further enhanced to 1.63 at room temperature. This improvement is attributed to the Hf atoms with lower phonon group velocity and higher electron effective mass, which result in a reduction in κ_{Tot} and an increase in the S. Finally, we propose a method for constructing the graphical superlattice vertical stacked heterostructure via laser ablation. By effectively reducing the κ_{Tot} of the structure, the ZT of the vertical heterostructure can be enhanced to 0.85 at room temperature. Our work provides theoretical support for enhancing the thermoelectric performance of 2D materials.

Conflict of interest The authors have no conflicts to disclose.

Supporting information See the supplementary material provides

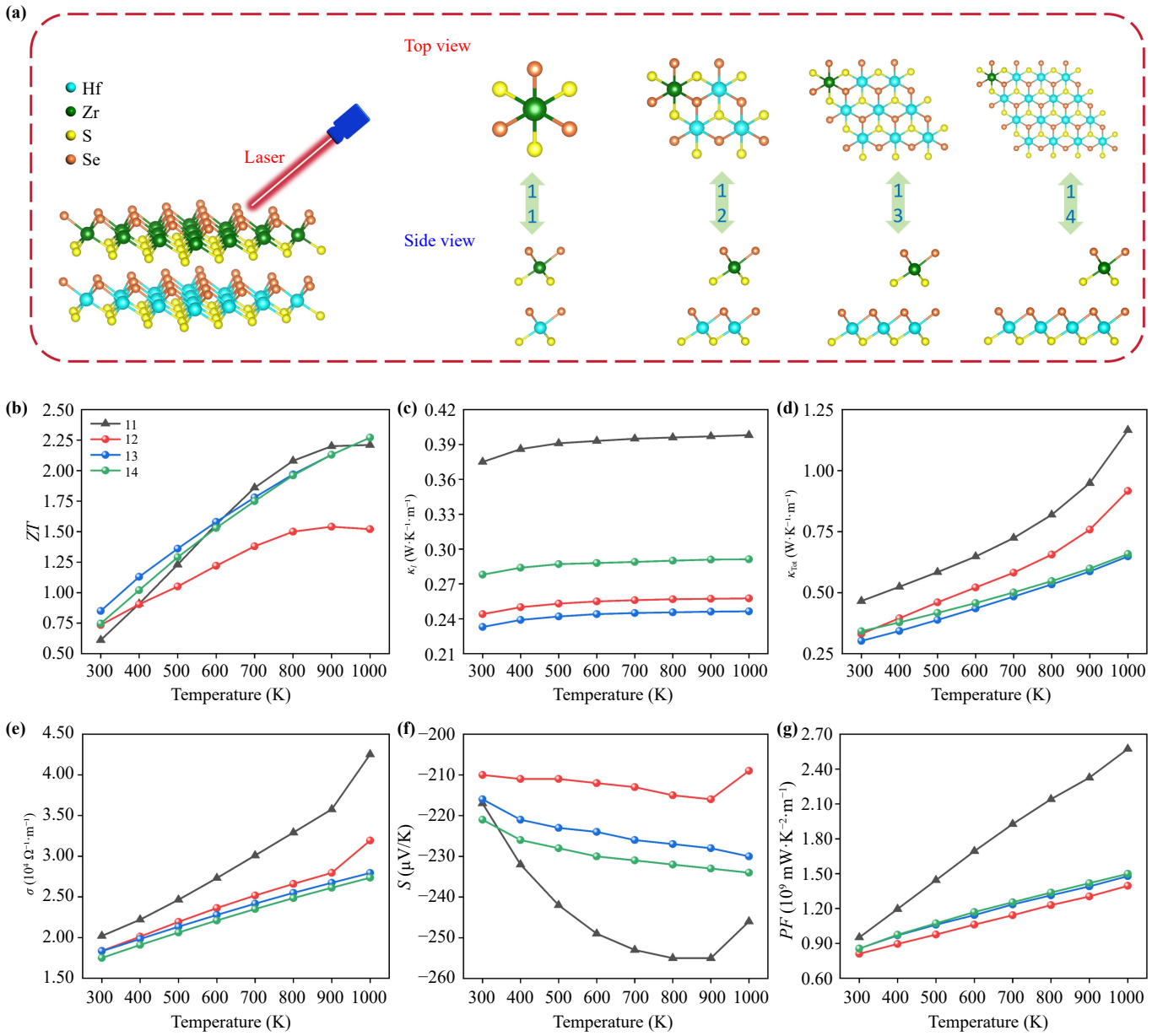

Fig. 5 Crystal structure and thermoelectric properties of the graphical superlattice vertical heterostructure. **(a)** Crystal structure of top and side view of a constructed the graphical superlattice by laser ablation. Function diagram of **(b)** optimal ZT; **(c)** κ_ι; **(d)** κ_{Tot}; **(e)** σ; **(f)** S and **(g)** PF with temperature for each structure.

detailed for various core materials at https://doi.org/10.15302/front-phys.2026.114203.

Data availability statement The data sets generated/analyzed during this study are available from the authors on reasonable request.

Acknowledgements This work was supported by the National Natural Science Foundation of China (Nos. 11874407, 91436102, and 11374353), the Natural Science Foundation for Youths of Inner Mongolia Autonomous Region (No. 2025QN01020), and Inner Mongolia University of Science and Technology Keju Talent Reserve Program (No. KJJH2024956).

References

1. B. Jiang, W. Wang, S. Liu, Y. Wang, C. Wang, Y. Chen, L. Xie, M. Huang, and J. He, High figure-of-merit and power generation in high-entropy GeTe-based thermoelectrics, *Science* 377(6602), 208 (2022)
2. J. Mao, G. Chen, and Z. Ren, Thermoelectric cooling materials, *Nat. Mater.* 20(4), 454 (2021)
3. B. H. Jia, D. Wu, L. Xie, W. Wang, T. Yu, S. Y. Li, Y. Wang, Y. J. Xu, B. B. Jiang, Z. Q. Chen, Y. X. Weng, and J. Q. He, Pseudo-nanostructure and trapped-hole release induce high thermoelectric performance in PbTe, *Science* 384(6691), 81 (2024)

4. Q. Y. Yan and M. G. Kanatzidis, High-performance thermoelectrics and challenges for practical devices, *Nat. Mater.* 21(5), 503 (2022)
5. L. D. Zhao, S. H. Lo, Y. S. Zhang, H. Sun, G. J. Tan, C. Uher, C. Wolverton, V. P. Dravid, and M. G. Kanatzidis, Ultralow thermal conductivity and high thermoelectric figure of merit in SnSe crystals, *Nature* 508(7496), 373 (2014)
6. G. Tan, L. D. Zhao, and M. G. Kanatzidis, Rationally designing high-performance bulk thermoelectric materials, *Chem. Rev.* 116(19), 12123 (2016)
7. S. Liu, S. L. Bai, Y. Wen, J. Lou, Y. Z. Jiang, Y. C. Zhu, D. R. Liu, Y. C. Li, H. N. Shi, S. B. Liu, L. Wang, J. Q. Zheng, Z. Zhao, Y. X. Qin, Z. K. Liu, X. Gao, B. C. Qin, C. Chang, C. Chang, and L. D. Zhao, Quadruple-band synglisis enables high thermoelectric efficiency in earth-abundant tin sulfide crystals, *Science* 387(6730), 202 (2025)
8. T. Zhu, Y. Liu, C. Fu, J. P. Heremans, J. G. Snyder, and X. Zhao, Compromise and synergy in high-efficiency thermoelectric materials, *Adv. Mater.* 29(14), 1605884 (2017)
9. X. L. Shi, J. Zou, and Z. G. Chen, Advanced thermoelectric design: From materials and structures to devices, *Chem. Rev.* 120(15), 7399 (2020)
10. C. Chang, M. Wu, D. He, Y. Pei, C. F. Wu, X. Wu, H. Yu, F. Zhu, K. Wang, Y. Chen, L. Huang, J. F. Li, J. He, and L. D. Zhao, 3D charge and 2D phonon transports leading to high out-of-plane ZT in n-type SnSe crystals, *Science* 360(6390), 778 (2018)
11. D. H. Ren, Y. Wen, H. Zeng, X. Q. Feng, T. Zhang, Y. Zhang, L. S. Wang, Q. Li, M. Du, Z. Y. Zhou, J. Q. Yi, and J. He, Recent advances in growth, characterization, and application of two-dimensional multiferroic materials, *Front. Phys. (Beijing)* 20(4), 044302 (2025)
12. K. F. Mak, C. G. Lee, J. Hone, J. Shan, and T. F. Heinz, Atomically thin MoS_2: A new direct-gap semiconductor, *Phys. Rev. Lett.* 105(13), 136805 (2010)
13. A. B. Maghirang, Z. Q. Huang, R. A. B. Villaos, C. H. Hsu, L. Y. Feng, E. Florido, H. Lin, A. Bansil, and F. C. Chuang, Predicting two-dimensional topological phases in Janus materials by substitutional doping in transition metal dichalcogenide monolayers, *npj 2D Mater. Appl.* 3, 35 (2019)
14. Y. C. Cheng, Z. Y. Zhu, M. Tahir, and U. Schwingenschlögl, Spin-orbit–induced spin splittings in polar transition metal dichalcogenide monolayers, *Europhys. Lett.* 102(5), 57001 (2013)
15. A. Patel, D. Singh, Y. Sonvane, P. B. Thakor, and R. Ahuja, High thermoelectric performance in two-dimensional Janus monolayer material WS-X (X = Se and Te), *ACS Appl. Mater. Interfaces* 12(41), 46212 (2020)
16. H. H. Huang, Z. X. Sun, C. C. Hu, and X. F. Fan, Janus penta-PdSeTe: A two-dimensional candidate with highthermoelectric performance, *J. Alloys Compd.* 924, 166581 (2022)
17. T. T. Wang, F. Chi, and J. Liu, Thermoelectric effect in Janus monolayer InSSe, *J. Nanoelectron. Optoelectron* 16(1), 119 (2021)
18. C. Wang, Y. C. Chen, G. Y. Gao, K. Xu, and H. Z. Shao, Theoretical investigations of Janus WSeTe monolayer and related van der Waals heterostructures with promising thermoelectric performance, *Appl. Surf. Sci.* 593, 153402 (2022)
19. F. Guo, B. Cui, M. Guo, J. Wang, J. Cao, W. Cai, and J. Sui, Enhanced thermoelectric performance of SnTe alloy with Ce and Li co-doping, *Mater. Today Phys.* 11, 100156 (2019)
20. Y. Pei, A. D. LaLonde, N. A. Heinz, X. Shi, S. Iwanaga, H. Wang, L. Chen, and G. J. Snyder, Stabilizing the optimal carrier concentration for high thermoelectric efficiency, *Adv. Mater.* 23(47), 5674 (2011)
21. Y. Shang, Y. Q. Wu, S. Abdulkarim, and M. T. Sun, Enhancement of thermoelectric performance of the transition metal dichalcogenides materials by a specific pressure, *Rare Met.* 44(8), 5703 (2025)
22. N. Wang, J. C. Yue, S. Q. Guo, H. Zhang, S. L. Li, M. N. Cui, Y. H. Liu, and T. Cui, Pressure induced enhancement of anharmonicity and optimization of thermoelectric properties in n-type SnS, *Front. Phys. (Beijing)* 20(3), 034206 (2025)
23. A. Kumari, A. Nag, and J. Kumar, Strain engineering and thermoelectric performance of Janus monolayers of titanium dichalcogenides: A DFT study, *Comput. Mater. Sci.* 218, 111925 (2023)
24. Q. Xia, Y. S. Liu, and G. Y. Gao, Enhanced thermoelectric performance and reversed anisotropy in the Janus penta-PdSeTe monolayer via biaxial strain, *J. Mater. Chem. C* 13(11), 5689 (2025)
25. Y. Jiang, J. Dong, H. L. Zhuang, J. Yu, B. Su, H. Li, J. Pei, F. H. Sun, M. Zhou, H. Hu, J. W. Li, Z. Han, B. P. Zhang, T. Mori, and J. F. Li, Evolution of defect structures leading to high ZT in GeTe-based thermoelectric materials, *Nat. Commun.* 13(1), 6087 (2022)
26. Y. Shang, X. P. Pan, Y. X. Jia, Y. Q. Wu, and M. T. Sun, Effect of pressure on the thermoelectric performance of monolayer Janus MoSSe materials with different native vacancy defects, *Nanoscale* 17(22), 13861 (2025)
27. S. L. Bai, S. W. Tang, M. X. Wu, D. M. Luo, J. Y. Zhang, D. Wan, and S. B. Yang, Unravelling the thermoelectric properties and suppression of bipolar effect under strain engineering for the asymmetric Janus SnSSe and PbSSe monolayers, *Appl. Surf. Sci.* 599, 153962 (2022)
28. S. Z. Huang, C. G. Fang, Q. Y. Feng, B. Y. Wang, H. D. Yang, B. Li, X. Xiang, X. T. Zu, and H. X. Deng, Strain tunable thermoelectric material: Janus ZrSSe monolayer, *Langmuir* 39(7), 2719 (2023)
29. G. Özbal, R. T. Senger, C. Sevik, and H. Sevinçli, Ballistic thermoelectric properties of monolayer semiconducting transition metal dichalcogenides and oxides, *Phys. Rev. B* 100(8), 085415 (2019)
30. J. Bera, A. Betal, and S. Sahu, Spin orbit coupling induced enhancement of thermoelectric performance of HfX_2 (X = S, Se) and its Janus monolayer, *J. Alloys Compd.* 872, 159704 (2021)
31. G. Kresse and J. Furthmüller, Efficient iterative schemes for ab initio total-energy calculations using a plane-wave basis set, *Phys. Rev. B* 54(16), 11169 (1996)
32. G. Kresse and J. Furthmüller, Efficiency of ab-initio total energy calculations for metals and semiconductors using a plane-wave basis set, *Comput. Mater. Sci.* 6(1),

15 (1996)
33. B. Hammer, L. B. Hansen, and J. K. Norskov, Improved adsorption energetics within density-functional theory using revised Perdew–Burke–Ernzerhof functionals, *Phys. Rev. B* 59(11), 7413 (1999)
34. S. Grimme, Semiempirical GGA-type density functional constructed with a long-range dispersion correction, *J. Comput. Chem.* 27(15), 1787 (2006)
35. W. Huang, X. Luo, C. K. Gan, S. Y. Quek, and G. Liang, Theoretical study of thermoelectric properties of few-layer MoS_2 and WSe_2, *Phys. Chem. Chem. Phys.* 16(22), 10866 (2014)
36. J. L. Alonso, X. Andrade, P. Echenique, F. Falceto, D. Prada-Gracia, and A. Rubio, Efficient formalism for large-scale ab initio molecular dynamics based on time-dependent density functional theory, *Phys. Rev. Lett.* 101(9), 096403 (2008)
37. M. Brandbyge, J. L. Mozos, P. Ordejón, J. Taylor, and K. Stokbro, Density-functional method for nonequilibrium electron transport, *Phys. Rev. B* 65(16), 165401 (2002)
38. J. Taylor, H. Guo, and J. Wang, Ab initio modeling of quantum transport properties of molecular electronic devices, *Phys. Rev. B* 63(24), 245407 (2001)
39. F. Li, W. Wei, H. Wang, B. Huang, Y. Dai, and T. Jacob, Intrinsic electricfield-induced properties in Janus MoSSe van der Waals structures, *J. Phys. Chem. Lett.* 10(3), 559 (2019)
40. S. D. Guo, X. S. Guo, R. Y. Han, and Y. Deng, Predicted Janus SnSSe monolayer: A comprehensive first-principles study, *Phys. Chem. Chem. Phys.* 21(44), 24620 (2019)
41. Y. Shang, Y. Q. Wu, and M. T. Sun, The super raman intensity induced by spin–orbit coupling effect in monolayer MoS_2 and WS_2 under varying pressures, *Mater. Today Phys.* 46, 101507 (2024)
42. M. Abdulsalam, E. Rugut, and D. P. Joubert, Mechanical, thermal and thermoelectric properties of MX_2 (M=Zr, Hf; X=S, Se), *Mater. Today Commun.* 25, 101434 (2020)
43. R. T. Sibatov and D. A. Timkaeva, Tunable electronic, optical and thermoelectric properties of stable quasi-fractal graphene/h-BN in-plane heterostructures, *FlatChem* 55, 100977 (2026)
44. Y. Ouyang, Y. Xie, Z. Zhang, Q. Peng, and Y. Chen, Very high thermoelectric figure of merit found in hybridtransition-metal-dichalcogenides, *J. Appl. Phys.* 120(23), 235109 (2016)
45. J. H. Kim, S. Y. Kim, Y. C. Cho, H. J. Park, H. J. Shin, S. Y. Kwon, and Z. H. Lee, Interface-driven partial dislocation formation in 2D heterostructures, *Adv. Mater.* 31(15), 1807486 (2019)
46. Y. C. Lin, J. K. Karthikeyan, Y. P. Chang, S. S. Li, S. Kretschmer, H. P. Komsa, P. W. Chiu, A. V. Krasheninnikov, and K. Suenaga, Formation of highly doped nanostripes in 2D transition metal dichalcogenides via a dislocation climb mechanism, *Adv. Mater.* 33(12), 2007819 (2021)
47. R. Gupta, and C. Bera, Modeling thermoelectric properties of monolayer and bilayer WS_2 by including intravalley and intervalley scattering mechanisms, *Phys. Rev. B* 108(11), 115406 (2023)
48. C. Liu, M. Yao, J. Yang, J. Xi, and X. Ke, Strong electron–phonon interaction induced significant reduction in lattice thermal conductivities for single-layer MoS_2 and PtSSe, *Mater. Today Phys.* 15, 100277 (2020)
49. H. Ogura, S. Kawasaki, Z. Liu, T. Endo, M. Maruyama, Y. L. Gao, Y. Nakanishi, H. E. Lim, K. Yanagi, T. Irisawa, K. Ueno, S. Okada, K. Nagashio, and Y. Miyata, In-plane heterostructures based on transition metal dichalcogenides for advanced electronics, *ACS Nano* 17(7), 6545 (2023)
50. X. Q. Zhang, C. H. Lin, Y. W. Tseng, K. H. Huang, and Y. H. Lee, Synthesis of lateral heterostructures of semiconducting atomic layers, *Nano Lett.* 15(1), 410 (2015)
51. M. Claassen, L. Xian, D. M. Kennes, and A. Rubio, Ultra-strong spin–orbit coupling and topological moiré engineering in twisted ZrS_2 bilayers, *Nat. Commun.* 13(1), 4915 (2022)
52. P. Yan, G. Y. Gao, G. Q. Ding, and D. Qin, Bilayer MSe_2 (M = Zr, Hf) as promising two-dimensional thermoelectric materials: A first-principles study, *RSC Adv.* 9(22), 12394 (2019)
53. N. Ghobadi, and S. B. Touski, The electrical and spin properties of monolayer and bilayer Janus HfSSe under vertical electrical field, *J. Phys.: Condens. Matter* 33(8), 085502 (2021)
54. J. Z. Song, and M. T. Sun, Modulating Thermoelectric Properties of the $MoSe_2/WSe_2$ Superlattice Heterostructure by Twist Angles, *ACS Appl. Mater. Interfaces* 16(3), 3325 (2024)
55. A. Castellanos-Gomez, M. Barkelid, A. M. Goossens, V. E. Calado, H. S. J. van der Zant, and G. A. Steele, Laser-thinning of MoS_2: On demand generation of a single-layer semiconductor, *Nano Lett.* 12(6), 3187 (2012)
56. S. M. Akkanen, H. A. Fernandez, and Z. Sun, Optical modification of 2D materials: Methods and applications, *Adv. Mater.* 34(19), 2110152 (2022)